



# rGO-Embedded Polymer Nanocomposite Layer for Improved Performance of Triboelectric Nanogenerator

Shilpa Rana<sup>1</sup> · Bharti Singh<sup>1</sup>

Received: 7 January 2024 / Accepted: 29 August 2024  
© The Minerals, Metals & Materials Society 2024

## Abstract

A triboelectric nanogenerator (TENG) working on a contact electrification and electrostatic induction principle is a promising energy source for fulfilling the energy demand of low power electronic devices by converting the ambient mechanical energy to useful electrical energy. Here, a polymer nanocomposite film-based triboelectric nanogenerator has been designed by embedding reduced graphene oxide (rGO) nanosheets in a polyvinylidene fluoride (PVDF) matrix as one of the friction layers. The PVDF nanocomposite film-based TENG was constructed and examined for structural, electrical, and surface properties with varied weight percentages of rGO nanofillers (0.0 wt%, 0.5 wt%, 1.0 wt%, 1.5 wt%, and 2.0 wt%). The experimental results demonstrate that the addition of rGO in a PVDF matrix considerably increased the output performance of the TENG device. The TENG device with 1.5 wt% of rGO can deliver the maximum output voltage and current of 95.9 V, and 16.8  $\mu$ A, respectively, which are  $\sim 3$  and  $\sim 7$  times the voltage and current produced by pristine PVDF film-based TENG. The enhanced performance of the nanogenerator is attributed to the addition of conductive nanofillers in the polymer matrix which improves the surface charge density of polymer nanocomposite films by forming a conduction network, resulting in more effective charge transfer. Moreover, the output of the nanogenerator is stored in the capacitor and used to drive commercial LEDs, revealing the TENGs' potential applications for designing self-powered electronic devices.

**Keywords** Triboelectrification · Nanogenerator · Energy harvesting · rGO

## Introduction

The global energy crisis with the technological advancement and increase in the human population has become one of the major problems that has motivated researchers all over the world to actively seek for innovative solutions to generate electricity from unconventional renewable energy sources. In light of this, various technologies have been developed and studies are still ongoing to harvest energy from sustainable energy sources, such as solar, thermal, vibration, wind, etc.<sup>1–4</sup> Among these technologies, triboelectric nanogenerators (TENGs) operating on the principle of triboelectrification and electrostatic induction have garnered considerable attention as an innovative

technology which converts mechanical energy from diverse sources into electrical energy. Because of their working principle, TENGs possess several advantages over other energy-harvesting devices due to their outstanding performance in energy harvesting with strong output signals, cost-effectiveness, robustness, simple design, and abundant choice of materials.<sup>5–7</sup> Also, it is well known that the surface charge density of triboelectric materials has a significant impact on TENGs' output performance. Therefore, various methods have been adopted by researchers to improve the TENG performance, among which two major approaches are (1) to select a suitable friction material with markedly different polarities and structural optimization, as the performance of the device greatly depends on the structure and material selection, and (2) surface modification with micro-/nanostructure formation, doping composition, and charge injection to improve and regulate the friction ignition effect.<sup>8–10</sup> Many materials, organic, inorganic, polymer, etc., have been explored since the invention of the TENG in 2012, and their triboelectric series have been made in

✉ Bharti Singh  
bhartisingh@dtu.ac.in

<sup>1</sup> Department of Applied Physics, Delhi Technological University, Main Bawana Road, Delhi 110042, India

which polymers currently dominate the triboelectric series due to their high charge transfer capacity.<sup>11,12</sup> PVDF is one of the most versatile polymer materials which serves as the negative triboelectric layer in TENGs due to its high electronegativity and flexibility, which keeps PVDF in the frontline of polymers to integrate with TENGs.<sup>13–15</sup> Up to now, several methods have been used to boost the performance of PVDF-based TENGs by electrospinning, microstructure formation, and porous structure formation which increase the effective contact surface area of the PVDF.<sup>16</sup> Another possible way to enhance the output performance of PVDF-based TENGs is the addition of optimized concentrations of nanofillers in the polymer matrix.<sup>17–19</sup> It has been observed that reduced graphene oxide (rGO) is preferred over other materials because of its electron-trapping capabilities, good conductivity, and higher electronegativity which help in efficiently capturing external electrons.

Hence, in this study, we propose a polymer composite film-based TENG by coupling of PVDF nanocomposite film with nylon film. rGO nanosheets with different weight percentages (0.5 wt%, 1.0 wt%, 1.5 wt%, 2.0 wt%) were incorporated into a PVDF polymer matrix and subjected to structural and morphological characterization to confirm successful doping of the nanofiller into the polymer matrix. The TENG's electrical output performance was optimized by subjecting it to tapping via a dynamic shaker at different force and frequency parameters. A maximum voltage and current of 95.9 V and 16.8  $\mu$ A, respectively, was produced by a device with 1.5 wt% of rGO. Furthermore, the device's ability to harvest energy has been shown through capacitor charging and powering of LEDs. Thus, the present studies demonstrate an easy and efficient approach for boosting TENGs' performance by the addition of nanofillers, thus extending its potential application in self-powered and wearable devices.

## 2. Materials and Methods

First, graphene oxide (GO) was synthesized via a modified Hummers' method,<sup>20</sup> and rGO was synthesized using a hydrothermal method, as reported in our previous study.<sup>21</sup> Initially, an aqueous solution of GO (1.5 mg/mL) was subjected to ultrasonication to achieve a homogeneous dispersion of the GO. Subsequently, this prepared solution was transferred to an autoclave and heated to 180°C for 12 h. The resulting solution was then washed with distilled water and ethanol and kept in oven at 60°C overnight to obtain rGO powder. For the synthesis of the PVDF polymer nanocomposite films, various weight percentages of rGO (0.5 wt%, 1.0 wt%, 1.5 wt% and 2.0 wt%) were mixed in 10 ml of N,N-dimethylformamide (DMF) and stirred

vigorously until the rGO completely dispersed in the solvent. Then, 1 g of the PVDF powder was slowly added to the prepared solution of rGO-dispersed DMF and stirred for 30 min to form a homogenous composite solution. Using a micropipette, the prepared solutions were drop-casted onto glass substrates and dried in an oven at 90°C. After natural cooling of the oven, the films were immersed in distilled water to obtain free-standing composite films (Fig. 1). The same procedure was adopted for synthesis of the PVDF film without addition of rGO.

The nylon films were synthesized by phase-inversion processes reported by Soin et al.<sup>22</sup>

Furthermore, a TENG device was fabricated by assembling the PVDF and the PVDF/rGO nanocomposite with the nylon film in vertical contact separation mode. For this, the PVDF/rGO nanocomposite and nylon films were cut into 2 × 2 cm<sup>2</sup> and used as the two active triboelectric layers. Aluminum tape was applied to the back side of each film to act as electrodes, while copper wire was utilized to establish electrical connections.

## Characterization

The crystallinity of the synthesized powder and thin films were analyzed using x-ray diffraction (XRD; DY 3733 Analytical Xpert pro) with the Cu K $\alpha$  x-ray source of 1.54 Å wavelength. Fourier-transform infrared (FTIR; PerkinElmer spectrum-II) spectroscopy of the thin films was carried out to ascertain the amount of  $\beta$ -phase present in the polymer nanocomposite films and to verify the existence of various functional groups. Field-emission scanning electron microscopy (FESEM; Zeiss GeminiSEM 500) was used to analyze the surface morphology of the samples. Raman spectroscopy of the rGO was carried out using a WiTec alpha 300 RA spectrometer with a 514-nm wavelength laser. The dielectric measurements of the samples in the frequency range of 20 Hz–10<sup>4</sup> Hz were performed using an LCR meter. The output performance of the TENGs were analyzed using an MDO34 Tektronix Oscilloscope by tapping the nanogenerator with the Micron MV-0025 electrodynamic shaker with an MPA-0200 function generator. A Keithley 6514 electrometer was used to carry out the short-circuit current and charge measurements. A force sensor was used to measure the force applied on the TENGs.

## 4. Results and Discussions

Several characterizations techniques have been used to confirm successful synthesis of the rGO. Figure 2a illustrates the synthesized rGO sample's XRD pattern, which is dominated by two broad peaks at 25.4° and 43.5°

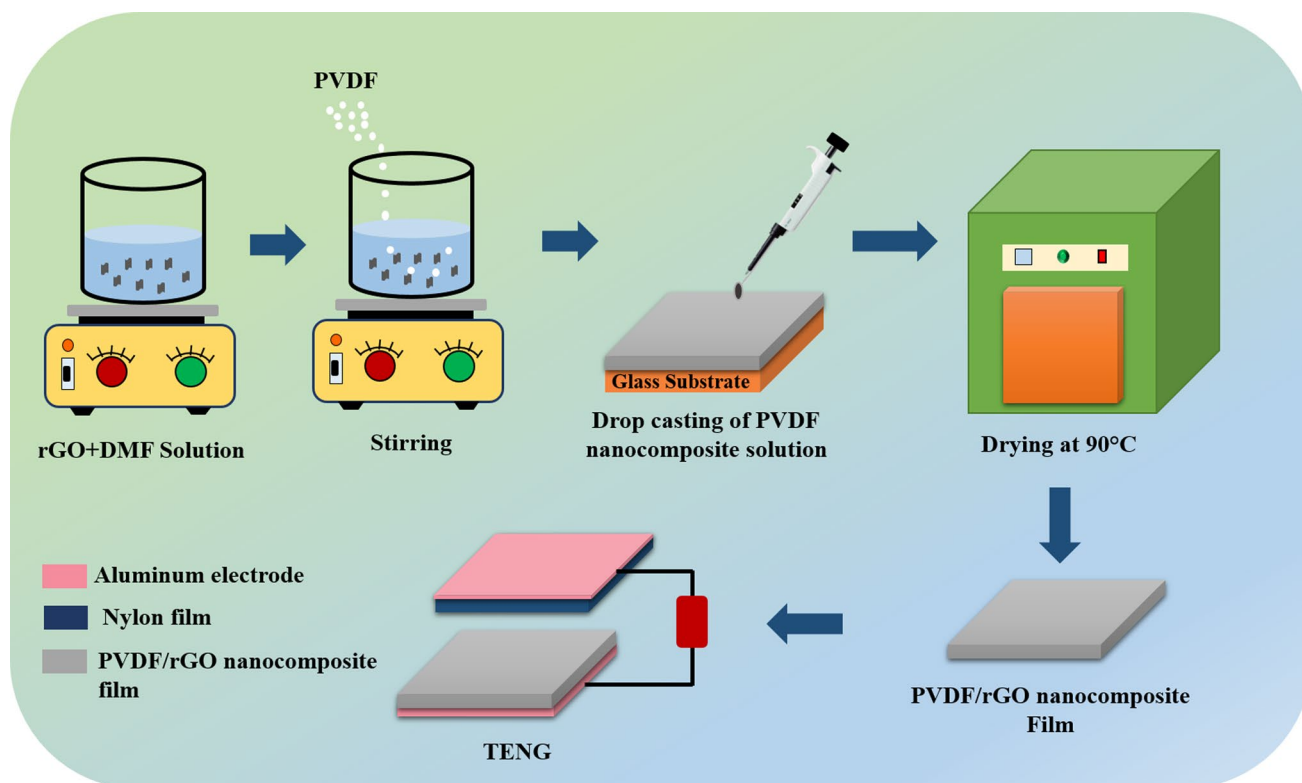


Fig. 1 Schematic showing the synthesis of PVDF/rGO nanocomposite film via drop-casting and fabrication of a TENG.

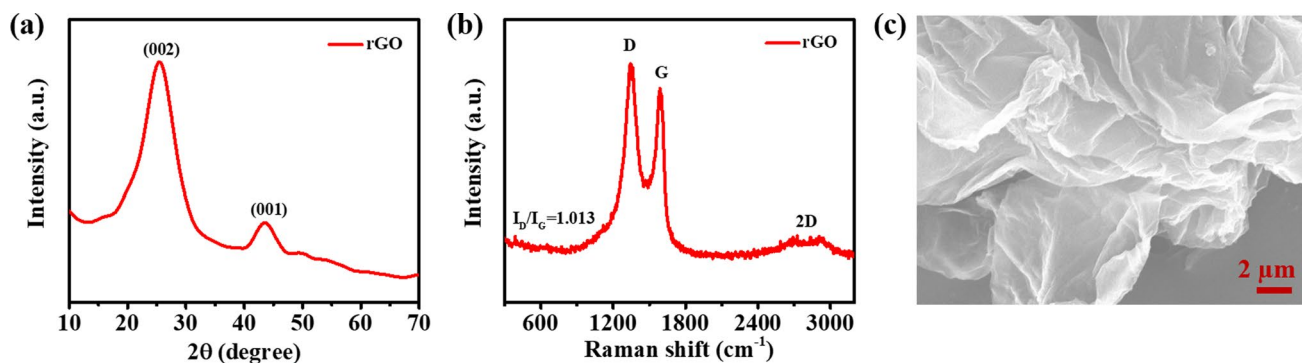


Fig. 2 (a) XRD pattern, (b) Raman spectra, and (c) FESEM micrograph of rGO.

corresponding to the (002) and (001) planes, respectively. The peak at  $25.4^\circ$  is attributed to the 2D structure of rGO, indicating that the  $\text{sp}^2$  network structure of graphene is formed during the reduction process. The peak's position and width indicate that GO was successfully reduced to rGO, which is consistent with the rGO's defective and amorphous structure. Additionally, a less intense peak at  $43.5^\circ$  can be observed, and this peak is associated with the turbostratic band of disordered carbon material.<sup>23,24</sup>

Raman spectroscopy is an effective technique that has been used widely to identify the structure, disorders,

defects, and the number of graphitic layers in carbon-based materials.<sup>25</sup> Raman spectra of rGO which consists mainly of two characteristic bands D and G band located at  $\sim 1347 \text{ cm}^{-1}$ , and  $\sim 1590 \text{ cm}^{-1}$ , respectively, are shown in Fig. 2b. The G band emerged from the in-plane vibrations of the  $\text{sp}^2$ -bonded carbon atoms, whereas the D band also referred to as the defective band is linked to structural defects. Furthermore, the intensity ratio of the D and G bands, i.e.,  $I_D/I_G$ , respectively, has been calculated to determine the degree of structural defects and disorder in the rGO, and has a value of 1.01 indicating that more defects are introduced

in the carbon structure and the effective reduction of GO to form rGO. In addition to two major peaks corresponding to D and G bands, a less intense broad 2D peak around  $2700\text{ cm}^{-1}$  is also observed, indicating the formation of multilayered graphene material.

FESEM was utilized to investigate the surface morphology of the rGO, and the corresponding FESEM micrograph is shown in Fig. 2c, demonstrating that rGO exhibits a laminated structure, comprising multiple thin sheets with distinct edges and a wrinkled texture spanning across the entire surface. These thin and semi-transparent layers revealed that rGO nanosheets are composed of multiple layers rather than a single layer, as in case of graphene.

Furthermore, synthesized rGO nanosheets with different concentrations of 0.0 wt%, 0.5 wt%, 1.0 wt%, 1.5 wt%, and 2.0 wt% rGO were mixed with PVDF to form the polymer nanocomposite films and were labeled P, PR1, PR2, PR3, and PR4, respectively. The crystallinity of PVDF and its composite films with varied concentrations of rGO (0 wt%, 0.5 wt%, 1.0 wt%, 1.5 wt%, and 2.0 wt%) were analyzed by XRD (Fig. 3a). All the films exhibit two characteristic peaks at diffraction angles of  $2\theta = 18.3^\circ$  and  $20.4^\circ$ , respectively.

The peak at  $18.3^\circ$  corresponds to the (020) reflection plane and is associated with the  $\alpha$  phase, whereas the peak at  $20.4^\circ$  is attributed to the  $\beta$  phase of the (110/200) reflection plane.<sup>25,26</sup> As we increased the concentration of rGO, the peak intensity associated with the  $\beta$  phase rose, but fell after 1.5 wt%. Furthermore, the peak conforming to rGO was not observed in the XRD spectra, which may be due to a relatively lower diffraction intensity and concentration of rGO in the PVDF nanocomposite film. For further better understanding of the crystallographic phase in the polymer nanocomposite films, FTIR spectroscopy was further used to quantify the rise in the content of the  $\beta$  phase of PVDF after doping it with rGO. Figure 3b shows that several vibrational groups are present in the FTIR spectra of the films, while absorbance peaks corresponding to different phases ( $\alpha$ ,  $\beta$ , and  $\gamma$  phases) are indicated in the spectra.<sup>27</sup> Moreover, when we doped rGO in the polymer matrix, the intensity of the peak corresponding to non-polar  $\alpha$  phase was diminished and the relative fraction of electroactive polar  $\beta$  phase was determined using:

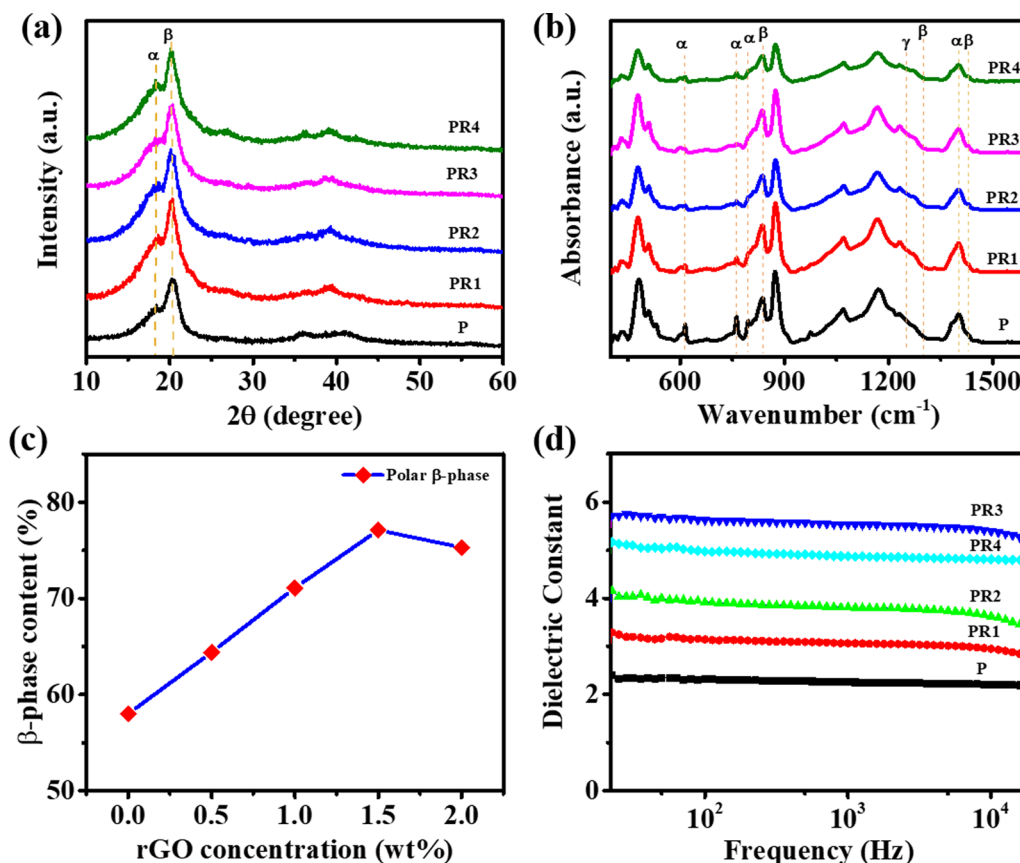


**Fig. 3** (a) XRD patterns, (b) FTIR spectra, (c) content of electroactive polar  $\beta$  phase, and (d) dielectric constant of PVDF nanocomposite films with different weight percentages of rGO.

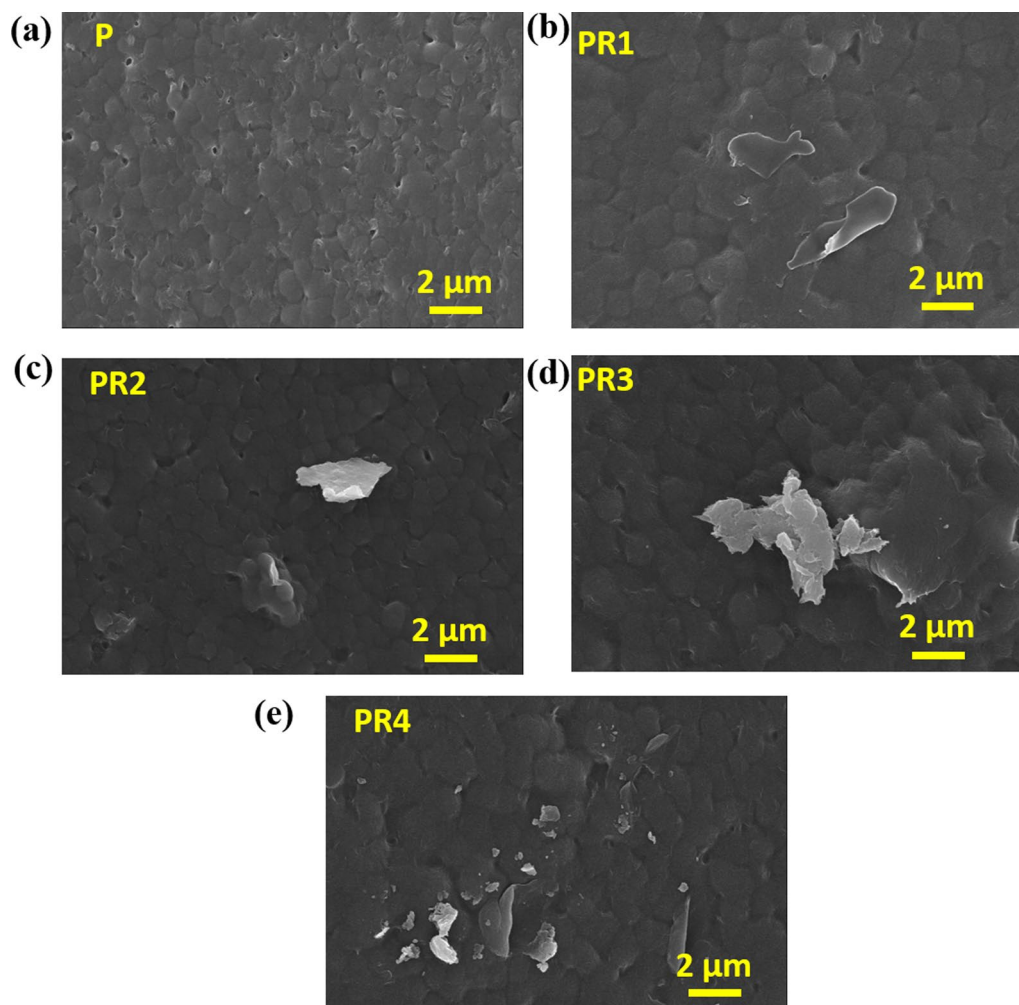


**Fig. 4** FESEM micrographs of (a–e) PVDF and PVDF nanocomposite films with varied concentrations of rGO.

$$F(\beta) = \frac{A_{\beta}}{1.26A_{\alpha} + A_{\beta}} \times 100\% \quad (1)$$

where  $A_{\alpha}$  and  $A_{\beta}$  are the absorption intensities at 762 and 840  $\text{cm}^{-1}$ , respectively. The calculated values of the relative fractions of the electroactive polar phase  $F(\beta)$  of P, PR1, PR2, PR3, and PR4 were 58%, 64.4%, 71.1%, 77.1%, and 75.3%, respectively, and the related results are illustrated in Fig. 3c. The percentage of the  $\beta$  phase content in the PVDF nanocomposite films was significantly enhanced with the increase in rGO concentration up to 1.5 wt%, while further addition of the nanofillers reduced its value. The possible reason behind the initial increase in the value of  $F(\beta)$  up to a certain concentration and thereafter decreasing can be understood by the fact that, when we add rGO in the PVDF matrix, the crystallinity of the nanocomposites first increases due to the interaction between surface charges (i.e., oxygen-containing functional group and delocalized  $\pi$  electrons) of rGO with the  $\text{CH}_2$  and  $\text{CF}_2$  dipoles of

PVDF which help in the gradual enhancement in the nucleation of the polar  $\beta$  phase by maximizing all trans molecular conformations.<sup>21,28</sup> However, after a certain concentration of rGO nanosheets (i.e., 1.5 wt% in our case), the alignment of the polymer chain became disturbed, resulting in suppressing the tendency of  $\beta$  phase formation arising because of a poor dipole arrangement in the PVDF chain.<sup>26,29</sup> Also, it has been reported in the literature that the dielectric constant of the triboelectric material is an important property which helps in improving the TENG device performance. Therefore, the dielectric constant of PVDF and its composite films were measured as a function of frequency with the help of the LCR meter (Fig. 3d). With increases in the rGO concentration, the dielectric constant of the PVDF film increases from 2.4 to 3.3, 4.1, 5.7, and 5.2 corresponding to the 0.5 wt%, 1.0 wt%, 1.5 wt%, and 2.0 wt%, respectively, of the rGO nanofillers. As expected, 1.5 wt% (i.e., PR3) has the maximum dielectric constant which is consistent with the XRD and FTIR studies. This increase

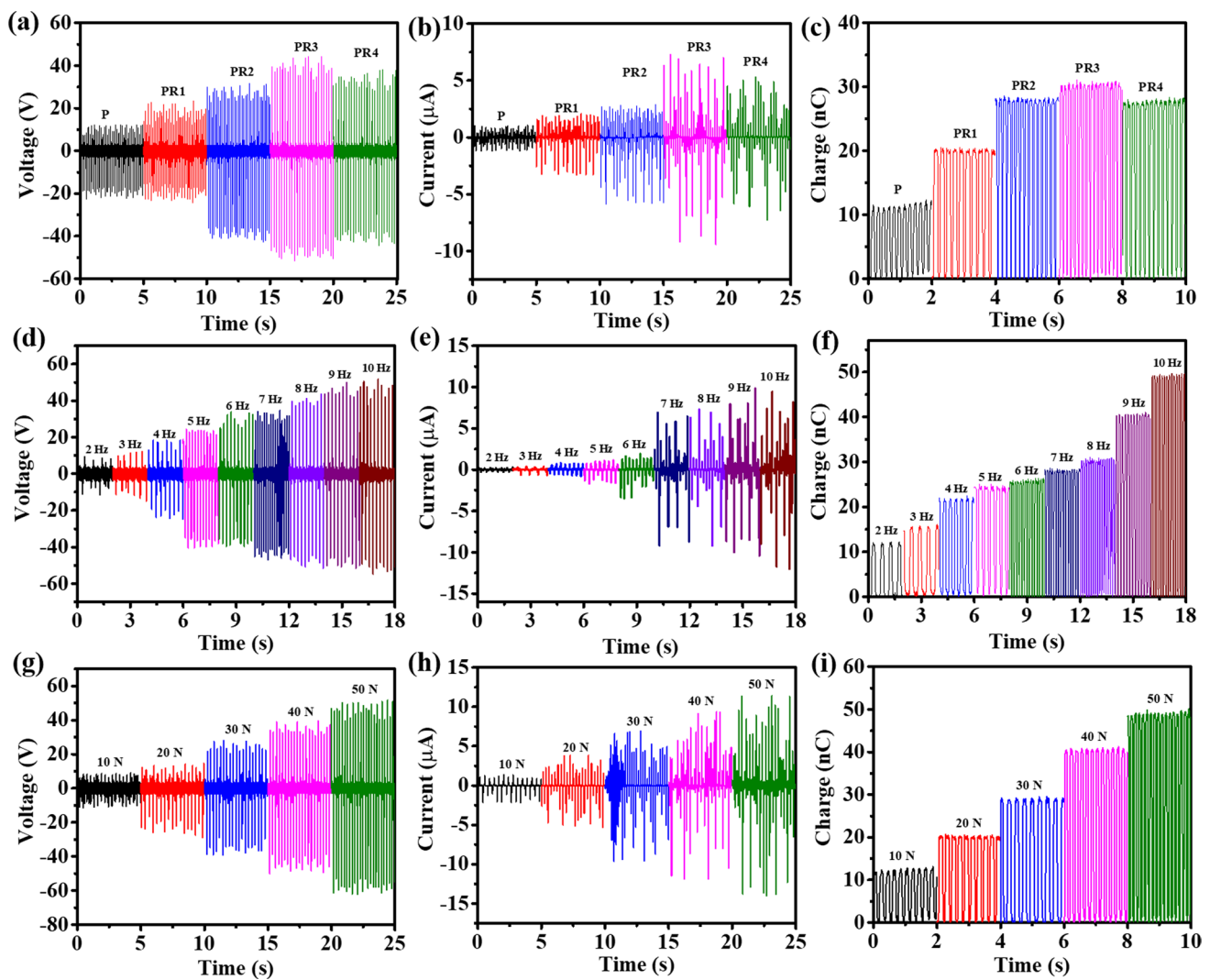


**Fig. 5** Measured open-circuit voltage, short-circuit current, and charge waveforms of the TENG obtained by (a–c) varying the concentration of rGO in the PVDF, (d–f) varying the input frequency, and (g–i) the impact force on the TENG with 1.5 wt% of rGO.

**Table 1** Comparison of PVDF/rGO-nylon-based TENG performance with various earlier reported TENGs.

Materials	Device area (cm <sup>2</sup> )	V <sub>oc</sub> (V)	I <sub>sc</sub> (μA)	Power density (μW/cm <sup>2</sup> )	Reference
PVC-rGO, aluminum	4.8 × 5	42.3	4.56	2.04	18
GO:PPy-PDMS, copper	–	27	0.359	–	32
CF-CNT, PTFE	2.5 × 2.5	60	1.8	11.06	33
SC-rGO, PTFE	3 × 3	81.5	–	255	34
PI/rGO, nylon	10 × 1.5	130	7.5	–	35
PDMS-rGO, water droplets	2 × 2	2	0.002	–	36
GO-AgNPs cellulose paper, PTFE	7.5 × 7.5	4	400	0.71	37
Ti@MoS <sub>2</sub> /PP, nylon	–	29.3	–	–	38
ZnONRs@CB/NF, PTFE	–	28	4.5	80	39
PVDF/rGO, nylon	2 × 2	95.9	16.8	95	This work

in dielectric constant value after the addition of nanofillers is due to the formation of microscopic dipole and micro

capacitor network formation which increases the capacitance of the nanocomposite film. However, the subsequent

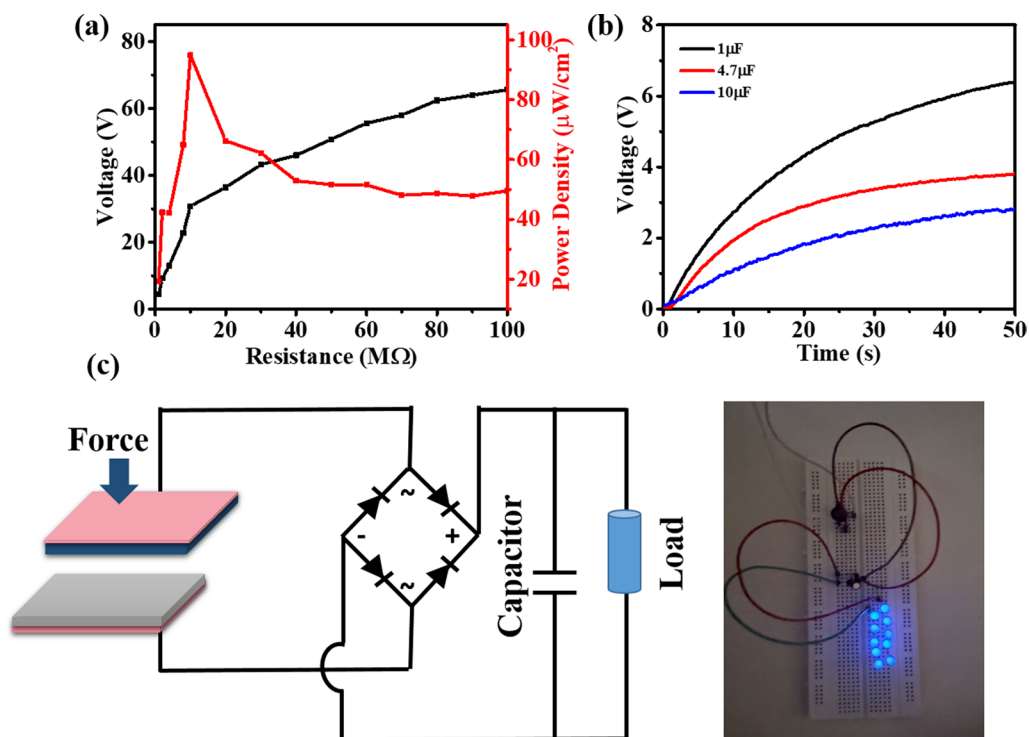


**Fig. 6** (a) Output voltage and power density as a function of load resistance, (b) charging of capacitors by a nanocomposite film-based TENG with 1.5 wt% of rGO, and (c) images of LEDs powered by TENGs with a schematic circuit diagram.

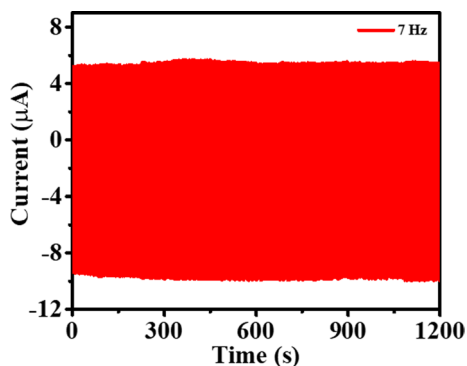


**Fig. 7** The durability of the PVDF/rGO TENG with 1.5 wt% of rGO.

decrease in value from 1.5 wt% to 2.0 wt% occurs due to the establishment of a conductive pathway, leading to a reduction in the film's capacitance. Hence, 1.5 wt% of the nanofillers is the optimum amount for the generation and retention of a significant quantity of triboelectric charges on the dielectric layer. The surface morphologies of PVDF and its composite films with varied concentrations of rGO are illustrated in Fig. 4a–e. It can be clearly seen from the figures that the rGO nanosheets are uniformly dispersed within the PVDF matrix without any agglomeration.

Figure 1 shows a schematic of the as-fabricated TENG formed by the coupling of PVDF and PVDF-rGO nanocomposite films with nylon as two highly negative and positive triboelectric layers operating in a simple vertical contact separation mode. In order to assess the TENG's performance, a series of tests were carried out by tapping nanogenerators with the help of an electrodynamic shaker. Initially, the electrical outputs including open-circuit voltage ( $V_{OC}$ ), short-circuit current ( $I_{SC}$ ) and transferred charges were measured with different concentrations of rGO, as depicted in Fig. 5a–c. A TENG with 1.5 wt% loading amount of rGO (i.e., the PR3-based TENG) generates the highest  $V_{OC}$ ,  $I_{SC}$ , and charges of 95.9 V, 16.8  $\mu\text{A}$ , and 28.1 nC in contrast to a pristine PVDF-based TENG which can generate  $V_{OC}$ ,  $I_{SC}$ , and charges of 35.4 V, 2.3  $\mu\text{A}$ , and 11.6 nC, while PR1, PR2, and PR4 film-based nanogenerators can produce  $V_{OC}$  and  $I_{SC}$  of 48.1 V, 74.9 V, 81.9 V, 5.4  $\mu\text{A}$ , 8.9  $\mu\text{A}$ , and 12.7  $\mu\text{A}$ , respectively. The maximum output performance of 1.5 wt% of rGO is also supported by the FTIR and dielectric studies which show the maximum content of the  $\beta$  phase and dielectric constant corresponding to 1.5 wt% of rGO doping in the PVDF matrix. Moreover, the impact of the input excitation force and frequency on the TENG output performance with 1.5 wt% of rGO (PR3) was also investigated and the corresponding  $V_{OC}$ ,  $I_{SC}$ , and charge waveforms are shown in Fig. 5d–i. The frequency of tapping

was also varied from 2 Hz to 10 Hz, with a highest value of voltage and current of  $\sim 107$  V and  $22 \mu\text{A}$  being attained at 10 Hz frequency. In the same vein, the impact of the applied force on the output capabilities of the TENG with 1.5 wt% rGO was explored through force variations ranging from 10 N to 50 N (Fig. 5g–i). At a forceful impact of 50 N, the TENG yielded a maximum voltage and current of around 113 V and  $20 \mu\text{A}$ , respectively. It is clearly illustrated from Fig. 5d–i that both the frequency and force follow similar rising patterns for voltage, current, and charge. The enhanced open-circuit voltage and short-circuit current in relation to the operating frequency and force may be attributed to the following reasons. First, the faster charge transfer at higher tapping frequency, and second, when we increase the impact force, there is an increase in the elastic deformation and effective contact area in the polymer nanocomposite film causing a rise in TENG capacitance which may be helpful in storing more triboelectric charges, and as a result improved the TENG performance.<sup>30,31</sup> Table I shows the comparison between the effect of nanofillers on the output performance of the TENG. To investigate the ideal output condition of the as-fabricated TENG, the generated voltage was also measured as a function of load resistance ranging from 1 M $\Omega$  to 100 M $\Omega$ , as shown in Fig. 6a. The optimal TENG can deliver a maximum power density of  $\sim 95 \mu\text{W}/\text{cm}^2$  across a matching load resistance of 10 M $\Omega$ . Furthermore, to confirm the practical energy-harvesting potential of the fabricated TENG, capacitors of 1.0  $\mu\text{F}$ , 4.7  $\mu\text{F}$ , and 10  $\mu\text{F}$  were charged by the PR3 film-based TENG after rectification. The corresponding voltage charging curves of capacitors are illustrated in Fig. 6b, showing the voltage buildup over a brief period during their charging process. According to the results, the 1  $\mu\text{F}$  capacitor demonstrated swift charging, reaching up to 6.4 V within 50 s. In contrast, the 4.7  $\mu\text{F}$  and 10  $\mu\text{F}$  capacitors only attained charges of 2.8 V and 3.8 V, respectively, within the same timeframe. Apart from charging the capacitor, the energy-harvesting performance of the TENG is illustrated via lighting of commercial LEDs and corresponding circuit diagram with an image of the LEDs shown in Fig. 6c. The video demonstration of the LEDs lighting with the help of the electrodynamic shaker is shown in Movie 1. The durability of the as-fabricated TENG is illustrated in Fig. 7, which shows excellent stable cyclic operation of TENG over 1200 cycles with negligible change in the value of the current. These results demonstrate the good durability of the TENG for long-term applications.

## Conclusions

We successfully fabricated PVDF/rGO nanocomposite film-based TENGs and examined the impact of rGO doping on TENG performance by coupling of PVDF

nanocomposite films with nylon film. The results showed that the addition of rGO in the PVDF matrix greatly improved the nucleation of crystalline  $\beta$  phase, dielectric, and charge transfer properties of PVDF film, resulting in the improved performance of the TENG device. A maximum voltage and current of 95.9 V, and  $16.8 \mu\text{A}$ , respectively, was obtained by the PR3 film-based TENG (i.e., 1.5 wt% of rGO), whereas a pristine PVDF film-based TENG could only generate 35.4 V voltage and  $2.4 \mu\text{A}$  current. Also, this device produced the highest power density of  $\sim 95 \mu\text{W}/\text{cm}^2$  when connected to a matching load resistance. The generated power was stored within the capacitor and employed to illuminate commercial LEDs, showing the potential application of TENGs in future low-power portable and wearable electronic devices.

**Supplementary Information** The online version contains supplementary material available at <https://doi.org/10.1007/s11664-024-11426-w>.

**Acknowledgments** The authors express their gratitude to CSIR (Award No. 08/133(042)/2019-EMR-I) for financial support that enabled the execution of this research endeavor.

**Conflict of interest** Authors asserts that they have no conflict of interest.

## References

1. Z. Kinas, A. Karabiber, A. Yar, A. Ozen, F. Ozel, M. Ersöz, and A. Okbaz, High-performance triboelectric nanogenerator based on carbon nanomaterials functionalized polyacrylonitrile nanofibers. *Energy* 239, 122369 (2022). <https://doi.org/10.1016/j.energy.2021.122369>.
2. S. Sripadmanabhan Indira, C. Aravind Vaithilingam, K.S.P. Oruganti, F. Mohd, and S.J.N. Rahman, Nanogenerators as a sustainable power source: state of art, applications, and challenges. *Nanomaterials* 9(5), 773 (2019). <https://doi.org/10.3390/nano9050773>.
3. C. Wu, A.C. Wang, W. Ding, H. Guo, and Z.L. Wang, Triboelectric nanogenerator: a foundation of the energy for the new era. *Adv. Energy Mater.* 9(1), 1802906 (2019). <https://doi.org/10.1002/aenm.201802906>.
4. H. Li, C.S.L. Koh, Y.H. Lee, Y. Zhang, G.C. Phan-Quang, C. Zhu, Z. Liu, Z. Chen, H.Y.F. Sim and C.L.J.N.E. Lay, A wearable solar-thermal-pyroelectric harvester: achieving high power output using modified rGO-PEI and polarized PVDF. *Nano Energy* 73, 104723 (2020). <https://doi.org/10.1016/j.nanoen.2020.104723>
5. C. Wu, T.W. Kim, and H.Y. Choi, Reduced graphene-oxide acting as electron-trapping sites in the friction layer for giant triboelectric enhancement. *Nano Energy* 32, 542 (2017). <https://doi.org/10.1016/j.nanoen.2016.12.035>.
6. D. Zhang, Z. Xu, Z. Yang, and X. Song, High-performance flexible self-powered tin disulfide nanoflowers/reduced graphene oxide nanohybrid-based humidity sensor driven by triboelectric nanogenerator. *Nano Energy* 67, 104251 (2020). <https://doi.org/10.1016/j.nanoen.2019.104251>.



7. K. Cheng, S. Wallaert, H. Ardebili, and A. Karim, Advanced triboelectric nanogenerators based on low-dimension carbon materials: a review. *Carbon* 194, 81 (2022). <https://doi.org/10.1016/j.carbon.2022.03.037>.
8. R. Mao, D. Zhang, Z. Wang, H. Zhang, D. Wang, M. Tang, L. Zhou, H. Cai, and H. Xia, Deep-learning-assisted low-cost flexible cotton yarn-based triboelectric nanogenerator for ultra-sensitive human-computer merging interfaces. *Nano Energy* 111, 108418 (2023). <https://doi.org/10.1016/j.nanoen.2023.108418>.
9. S.A. Lone, K.C. Lim, K. Kaswan, S. Chatterjee, K.-P. Fan, D. Choi, S. Lee, H. Zhang, J. Cheng, and Z.-H. Lin, Recent advancements for improving the performance of triboelectric nanogenerator devices. *Nano Energy* 99, 107318 (2022). <https://doi.org/10.1016/j.nanoen.2022.107318>.
10. Y. Zou, J. Xu, K. Chen, and J. Chen, Advances in nanostructures for high-performance triboelectric nanogenerators. *Adv. Mater. Technol.* 6(3), 2000916 (2021). <https://doi.org/10.1002/admt.202000916>.
11. H. Zou, Y. Zhang, L. Guo, P. Wang, X. He, G. Dai, H. Zheng, C. Chen, A.C. Wang, and C. Xu, Quantifying the triboelectric series. *Nat. Commun.* 10(1), 1427 (2019). <https://doi.org/10.1038/s41467-019-09461-x>.
12. G. Khandelwal, N.P. Maria Joseph Raj, and S.J. Kim, Materials beyond conventional triboelectric series for fabrication and applications of triboelectric nanogenerators. *Adv. Energy Mater.* 11(33), 2101170 (2021). <https://doi.org/10.1002/aenm.202101170>.
13. P. Pandey, D.-H. Jung, G.-J. Choi, M.-K. Seo, S. Lee, J.M. Kim, I.-K. Park, and J.I. Sohn, Nafion-mediated barium titanate-polymer composite nanofibers-based triboelectric nanogenerator for self-powered smart street and home control system. *Nano Energy* 107, 108134 (2023). <https://doi.org/10.1016/j.nanoen.2022.108134>.
14. M. Tayyab, J. Wang, J. Wang, M. Maksutoglu, H. Yu, G. Sun, F. Yildiz, M. Eginligil, and W. Huang, Enhanced output in polyvinylidene fluoride nanofibers based triboelectric nanogenerator by using printer ink as nano-fillers. *Nano Energy* 77, 105178 (2020). <https://doi.org/10.1016/j.nanoen.2020.105178>.
15. H.H. Singh and N. Khare, Flexible ZnO-PVDF/PTFE based piezo-tribo hybrid nanogenerator. *Nano Energy* 51, 216 (2018). <https://doi.org/10.1016/j.nanoen.2018.06.055>.
16. Y. Wang, Y. Yang, and Z.L. Wang, Triboelectric nanogenerators as flexible power sources. *npj Flex. Electron.* 1(1), 10 (2017). <https://doi.org/10.1038/s41528-017-0007-8>.
17. S. Rana, V. Singh, and B. Singh, Recent trends in 2D materials and their polymer composites for effectively harnessing mechanical energy. *iScience* (2022). <https://doi.org/10.1016/j.isci.2022.103748>.
18. R.F.S. Muktar Ahmed, S.B. Mohan, S.M. Ankanathappa, M. Shivanna, S.A. Basith, M.H. Chandrashekhara Shastry, A. Chandrasekhar, and K. Sannathammegowda, Sucrose assisted chemical-free synthesis of rGO for triboelectric nanogenerator: Green energy source for smart-water dispenser. *Nano Energy* 106, 108085 (2023). <https://doi.org/10.1016/j.nanoen.2022.108085>.
19. G.-Z. Li, G.-G. Wang, Y.-W. Cai, N. Sun, F. Li, H.-L. Zhou, H.-X. Zhao, X.-N. Zhang, J.-C. Han, and Y. Yang, A high-performance transparent and flexible triboelectric nanogenerator based on hydrophobic composite films. *Nano Energy* 75, 104918 (2020). <https://doi.org/10.1016/j.nanoen.2020.104918>.
20. D.C. Marcano, D.V. Kosynkin, J.M. Berlin, A. Sinitskii, Z. Sun, A. Slesarev, L.B. Alemany, W. Lu, and J.M. Tour, Improved synthesis of graphene oxide. *ACS Nano* 4(8), 4806 (2010). <https://doi.org/10.1021/nn1006368>.
21. S. Rana, V. Singh, and B. Singh, Tailoring the output performance of PVDF-based piezo-tribo hybridized nanogenerators via B, N-codoped reduced graphene oxide. *ACS Appl. Electron. Mater.* 4(12), 5893 (2022). <https://doi.org/10.1021/acsaelm.2c01085>.
22. N. Soin, P. Zhao, K. Prashanthi, J. Chen, P. Ding, E. Zhou, T. Shah, S.C. Ray, C. Tsonos, T. Thundat, E. Siores, and J. Luo, High performance triboelectric nanogenerators based on phase-inversion piezoelectric membranes of poly(vinylidene fluoride)-zinc stannate (PVDF-ZnSnO<sub>3</sub>) and polyamide-6 (PA6). *Nano Energy* 30, 470 (2016). <https://doi.org/10.1016/j.nanoen.2016.10.040>.
23. N. Díez, A. Śliwak, S. Gryglewicz, B. Grzyb, and G. Gryglewicz, Enhanced reduction of graphene oxide by high-pressure hydrothermal treatment. *RSC Adv.* 5(100), 81831 (2015). <https://doi.org/10.1039/C5RA14461B>.
24. S. Shukla, I. Khan, V.K. Bajpai, H. Lee, T. Kim, A. Upadhyay, Y.S. Huh, Y.-K. Han, and K.M. Tripathi, Sustainable graphene aerogel as an ecofriendly cell growth promoter and highly efficient adsorbent for histamine from red wine. *ACS Appl. Mater. Interfaces* 11(20), 18165 (2019). <https://doi.org/10.1021/acami.9b02857>.
25. A. Anand, D. Meena, K.K. Dey, and M.C. Bhatnagar, Enhanced piezoelectricity properties of reduced graphene oxide (RGO) loaded polyvinylidene fluoride (PVDF) nanocomposite films for nanogenerator application. *J. Polym. Res.* 27(12), 1 (2020). <https://doi.org/10.1007/s10965-020-02323-x>.
26. S.K. Karan, D. Mandal, and B.B. Khatua, Self-powered flexible Fe-doped RGO/PVDF nanocomposite: an excellent material for a piezoelectric energy harvester. *Nanoscale* 7(24), 10655 (2015). <https://doi.org/10.1039/C5NR02067K>.
27. X. Cai, T. Lei, D. Sun, and L. Lin, A critical analysis of the  $\alpha$ ,  $\beta$  and  $\gamma$  phases in poly(vinylidene fluoride) using FTIR. *RSC Adv.* 7(25), 15382 (2017). <https://doi.org/10.1039/C7RA01267E>.
28. S. Rana, and B. Singh, Polymer nanocomposite film based piezoelectric nanogenerator for biomechanical energy harvesting and motion monitoring. *J. Mater. Sci. Mater. Electron.* 34(25), 1764 (2023). <https://doi.org/10.1007/s10854-023-11207-x>.
29. R. Bhunia, S. Gupta, B. Fatma, Prateek, R.K. Gupta and A. Garg, Milli-Watt Power harvesting from dual triboelectric and piezoelectric effects of multifunctional green and robust reduced graphene oxide/P(VDF-TrFE) composite flexible films. *ACS Appl. Mater. Interfaces* 11(41), 38177 (2019). <https://doi.org/10.1021/acami.9b13360>.
30. L. Shi, H. Jin, S. Dong, S. Huang, H. Kuang, H. Xu, J. Chen, W. Xuan, S. Zhang, and S. Li, High-performance triboelectric nanogenerator based on electrospun PVDF-graphene nanosheet composite nanofibers for energy harvesting. *Nano Energy* 80, 105599 (2021). <https://doi.org/10.1016/j.nanoen.2020.105599>.
31. T. Bhatta, P. Maharjan, H. Cho, C. Park, S.H. Yoon, S. Sharma, M. Salauddin, M.T. Rahman, S.M.S. Rana, and J.Y. Park, High-performance triboelectric nanogenerator based on MXene functionalized polyvinylidene fluoride composite nanofibers. *Nano Energy* 81, 105670 (2021). <https://doi.org/10.1016/j.nanoen.2020.105670>.
32. E.J. Jelmy, D. Jose, K.V. Vijoy, K.J. Saji, and H. John, Enhanced triboelectric performance of graphene oxide-conducting polymer hybrid modified polydimethylsiloxane composites. *Mater. Adv.* 3(17), 6897 (2022). <https://doi.org/10.1039/D2MA00771A>.
33. G.M. Rani, C.-M. Wu, K.G. Motora, R. Umaphathi, and C.R.M. Jose, Acoustic-electric conversion and triboelectric properties of nature-driven CF-CNT based triboelectric nanogenerator for mechanical and sound energy harvesting. *Nano Energy* 108, 108211 (2023). <https://doi.org/10.1016/j.nanoen.2023.108211>.
34. H.J. Hwang, J.S. Yeon, Y. Jung, H.S. Park, and D. Choi, Extremely foldable and highly porous reduced graphene oxide films for shape-adaptive triboelectric nanogenerators. *Small* 17(9), 1903089 (2021). <https://doi.org/10.1002/sml.201903089>.

35. X. Zhao, B. Chen, G. Wei, J.M. Wu, W. Han, and Y. Yang, Polyimide/graphene nanocomposite foam-based wind-driven triboelectric nanogenerator for self-powered pressure sensor. *Adv. Mater. Technol.* 4(5), 1800723 (2019). <https://doi.org/10.1002/admt.201800723>.
36. A.N. Parvez, M.H. Rahaman, H.C. Kim, and K.K. Ahn, Optimization of triboelectric energy harvesting from falling water droplet onto wrinkled polydimethylsiloxane-reduced graphene oxide nanocomposite surface. *Compos. B Eng.* 174, 106923 (2019). <https://doi.org/10.1016/j.compositesb.2019.106923>.
37. A.A. Pillai, J. John, R.M. Mathew, J. Jose, E.S. Zacharia, R. Abraham, N.M. Johnson, R.L. Thomas, and V. Thomas, Enhanced output performance of graphene oxide based triboelectric nanogenerators via plasmon coupling. *Mater. Sci. Eng. B* 296, 116637 (2023). <https://doi.org/10.1016/j.mseb.2023.116637>.
38. S. Veeralingam and S. Badhulika, Ti@MoS<sub>2</sub> incorporated Polypropylene/Nylon fabric-based porous, breathable triboelectric nanogenerator as respiration sensor and ammonia gas sensor applications. *Sens. Actuators B Chem.* 380, 133346 (2023). <https://doi.org/10.1016/j.snb.2023.133346>.
39. N. Jayababu, and D. Kim, ZnO nanorods@conductive carbon black nanocomposite based flexible integrated system for energy conversion and storage through triboelectric nanogenerator and supercapacitor. *Nano Energy* 82, 105726 (2021). <https://doi.org/10.1016/j.nanoen.2020.105726>.

**Publisher's Note** Springer Nature remains neutral with regard to jurisdictional claims in published maps and institutional affiliations.

Springer Nature or its licensor (e.g. a society or other partner) holds exclusive rights to this article under a publishing agreement with the author(s) or other rightsholder(s); author self-archiving of the accepted manuscript version of this article is solely governed by the terms of such publishing agreement and applicable law.